Assessment of multidrug resistance on cell coculture patterns using scanning electrochemical microscopy

Sabine Kuss[a,b,1], David Polcari[b,1], Matthias Geissler[c], Daniel Brassard[c], and Janine Mauzeroll[a,b,2]

[a]Department of Chemistry, Université du Québec à Montréal, Montreal, QC, Canada H2X 2J6; [b]Department of Chemistry, McGill University, Montreal, QC, Canada H3A 0B8; and [c]National Research Council of Canada, Boucherville, QC, Canada J4B 6Y4

Edited[†] by Allen J. Bard, The University of Texas at Austin, Austin, TX, and approved April 15, 2013 (received for review August 27, 2012)

The emergence of resistance to multiple unrelated chemotherapeutic drugs impedes the treatment of several cancers. Although the involvement of ATP-binding cassette transporters has long been known, there is no in situ method capable of tracking this transporter-related resistance at the single-cell level without interfering with the cell's environment or metabolism. Here, we demonstrate that scanning electrochemical microscopy (SECM) can quantitatively and noninvasively track multidrug resistance-related protein 1–dependent multidrug resistance in patterned adenocarcinoma cervical cancer cells. Nonresistant human cancer cells and their multidrug resistant variants are arranged in a side-by-side format using a stencil-based patterning scheme, allowing for precise positioning of target cells underneath the SECM sensor. SECM measurements of the patterned cells, performed with ferrocenemethanol and $[Ru(NH_3)_6]^{3+}$ serving as electrochemical indicators, are used to establish a kinetic "map" of constant-height SECM scans, free of topography contributions. The concept underlying the work described herein may help evaluate the effectiveness of treatment administration strategies targeting reduced drug efflux.

microelectrode | MRP1 | HeLa cells

Cancer cells, such as lung cancer or leukemia, acquire resistance to multiple unrelated drugs in response to treatment with chemotherapeutic agents (1, 2). Resistance impedes therapeutic effectiveness, which in turn, reduces the long-term survival rate of cancer patients (2). The emergence of multidrug resistance (MDR) involves the overexpression of transmembrane proteins P-glycoprotein (P-gp) and MDR-related protein 1 (MRP1), which both belong to the family of 5′-triphosphate-binding cassette transporters (known as ABC transporters). P-gp and MRP1 act as molecular "pumps," actively removing therapeutic agents from the cancer cells, thereby preventing the drug from inducing the desired effect on the cell nucleus or cytoplasm. MDR based on P-gp is relatively well understood and involves binding of hyaluronan to the cell surface glycoprotein CD44. The resulting up-regulation of the transcriptional cofactor p300 expression and therefore the NFkappaB-specific transcriptional up-regulation lead to the production of P-gp, and with that chemoresistance in cells (3). However, the mechanism that causes MRP1-mediated MDR remains unclear.

Currently, quantification of MDR relies on immunohistochemical analyses, such as real-time PCR, focusing mostly on P-gp or other members of ABC transporters (4–9). Fluorescent MRP1-specific studies were also conducted, revealing that resistant and nonresistant cancer cells have differential intracellular content of glutathione and GST, which affect their cell death mechanism during hyperthermia (10). Microvoltammetry was also used to measure the efflux of chemotherapeutic drugs from normal and MDR cancer cells on the single-cell level, with detection limits in the nanomolar range (11). Finally, flow cytometry has routinely been used to quantify and compare expression levels and activity of different ABC transporters that are linked to MDR (12–14). Although the transporter activity can be inferred from the drug retention in the cell, this method has been advanced by using the invariable drug retention on polymer beads as a standard in flow cytometry measurements (15). Herein, we report the use of cell coculture patterns for quantitative analysis of MDR in adenocarcinoma cervical cancer cells on the single-cell level using scanning electrochemical microscopy (SECM). In contrast with flow cytometric quantification of MDR, SECM allows for in situ observation on the single-cell level without interfering with the cell's environment or metabolism.

In SECM, a microelectrode is scanned across a surface while the electrochemical current is recorded with high spatial and temporal resolution (16). Since the first studies on single human cells emerged in 1998 (17), SECM has gained increasing attention as an analytical tool for biological studies (18–21). After successfully confirming cell viability and oxidative stress in living cells (22–24), the focus of analytical studies shifted toward the investigation of MDR. For example, the MRP1-mediated efflux of the menadione-S-glutathione conjugate (thiodione) was monitored in yeast and hepatoblastoma cells, making it possible to estimate the export rate of thiodione by SECM (24, 25). Most recently, Bard et al. monitored the formation of thiodione from menadione in adenocarcinoma cervical cancer cells (HeLa). In this study, the detection of thiodione by SECM not only allowed for the quantification of MRP1-mediated efflux of thiodione, but with the use of MK571 as an MRP1 blocker, the MRP1 efflux pump was identified as a major carrier for thiodione in living HeLa cells (26). The work presented in this study uses genetic modification of HeLa cells to compare a wild-type culture with MRP1 overexpressing cells (HeLa-R). The redox mediator ferrocenemethanol ($FcCH_2OH$) is used to quantify MRP1 activity of these two cell lines through its unique interaction with glutathione, a peptide molecule involved in MRP1-related transport. Tracking the evolution of MRP1 activity and expression is important because direct clinical implications make MRP1 a relatively unique molecular marker in comparison with other prognostic variables identified for several cancer types (27, 28).

Results and Discussion

Patterning of Cell Islands. Comparative SECM measurements on the single-cell level benefit from culture substrates that allow for arrangement of cells in a regular format. A consistent template providing alignment and registration between cells (as opposed to a random distribution) makes it possible to perform measurements multiple times and achieve a high level of reliability. In addition, it facilitates the positioning of cells underneath the microelectrode, thereby reducing preparation and analysis time. Because growth of cells largely depends on the properties of the surface on which they grow, template formation generally requires

Author contributions: S.K., D.P., M.G., and J.M. designed research; S.K. and D.P. performed research; D.B. contributed new reagents/analytic tools; S.K., D.P., and J.M. analyzed data; and S.K., D.P., M.G., and J.M. wrote the paper.

The authors declare no conflict of interest.

[†]This Direct Submission article had a prearranged editor.

Freely available online through the PNAS open access option.

[1]S.K. and D.P. contributed equally to this work.

[2]To whom correspondence should be addressed. E-mail: janine.mauzeroll@mcgill.ca.

This article contains supporting information online at www.pnas.org/lookup/suppl/doi:10.1073/pnas.1214809110/-/DCSupplemental.

a patterning step to be performed with the substrate. One approach involves activation of selected regions on a nonresponsive surface. A number of modification schemes involving self-assembled monolayers (29, 30), polymer films (31), and proteins (32) have been shown to direct cell attachment on a variety of natural and artificial substrates. Another approach relies on masking selected sites on an active surface to prevent adhesion of cells in these regions. The use of microfluidic systems (33, 34) and stencil masks (35, 36) are examples of this approach. Both methodologies take advantage of topographic features that provide a physical barrier in the patterning process. Even though many techniques are readily applicable to the patterning of a single cell line, they often fail to be effective when two (or more) cell lines are to be considered for array formation, especially at reduced scale.

Herein, we describe a stencil-based patterning approach that constitutes a practical solution to this end. We use an open through-hole membrane fabricated from an elastomeric block-copolymer (e.g., Versaflex CL30, GLS Corp.) (37) (see *SI Text* for details) in combination with oxygen plasma treatment to achieve live cell patterns on an insulating plastic substrate (e.g., Zeonor 1060R, Zeon Chemicals). Versaflex CL30 is a melt-processable styrenic ethylene/butylene block-copolymer (38, 39) which has recently been shown to promote the fabrication of thin-film membranes with small-scale openings in a single step using hot embossing lithography (HEL) (37). In principle, open through-hole membranes can be produced from other elastomers such as poly(dimethylsiloxane) (PDMS), which to this end constitutes the prime material for soft microfabrication and patterning (35, 36). However, the method described herein provides several advantages with respect to fabrication and handling of the membranes (37). For example, Versaflex CL30 provides off-the-shelf availability as it can be stored (e.g., as an extruded sheet) over extended periods of time, whereas PDMS as a thermoset polymer necessitates timely preparation. Thin, open through-hole membranes obtained with standard PDMS formulations (e.g., Sylgard 184) are relatively fragile, which makes their handling nontrivial and limits the scope of possible applications. Versaflex CL30, on the other hand, provides superior mechanical stability as reflected by 780% elongation at break (whereas PDMS generally does not exceed 140%), diminishing the risk of damage during removal from the mold and providing the possibility of reducing vertical and lateral dimensions of the replicated features. Spin-casting of PDMS further contributes to irregularities in thickness of the membrane (40), whereas those fabricated from Versaflex CL30 using HEL are smooth and uniform in thickness, with the embossed open through-holes showing excellent lithographic definition. We produced membranes with openings ranging from 50 to 500 μm, as shown in Fig. 1 *A* and *B*. Openings are used to form oxygen plasma-treated spots (OPS) on Zeonor serving as a solid cell culture substrate. Previous work has shown that hydrophilic, oxygen-containing groups promote cell attachment on a Zeonor surface (33). Each membrane made it possible to achieve cell islands with different dimensions, as shown for both HeLa (Fig. 1 *C–E*) and HeLa-R cells (Fig. 1 *F–H*). However, the details of the patterning process must be adjusted for each cell line according to morphology and characteristics of growth. For example, HeLa cells are more efficiently patterned on OPS provided by an untreated membrane that is placed on the Zeonor slide following exposure to oxygen plasma. Due to their tendency to grow in colonies, HeLa-R cells are preferably seeded on a Zeonor substrate from which the membrane was removed upon oxygen plasma treatment. Regardless of the option used, formation of OPS benefits from the ability of the elastomeric membrane to achieve intimate, yet reversible contact with the substrate (37). OPS ranging from 200 to 400 μm in diameter enable cell growth in defined, well-populated islands, whereas 50-μm OPS (either circular or rectangular) result in groups with a limited number (e.g., 2–9 cells) for both HeLa and HeLa-R cell lines. The defined physical separation of cells provides control over several experimental parameters, such as location of target cells, cell movement during acquisition, and analysis time (which can be extended to at least 8 h). Studies on cell communication or cell signaling, observation of cell death, and examination of the cell response to drugs or other medical treatments will benefit from this patterning procedure.

SECM Imaging. We performed SECM measurements on patterned HeLa cells using a Pt microelectrode biased at a potential where the dissolved redox mediator $FcCH_2OH$ is oxidized to $[FcCH_2OH]^+$ (Scheme S1) under mass-transfer control. Fig. 2*A* represents a redox reactant competition mode to illustrate electrochemical reactions during SECM measurements. In this scheme, the reactant $FcCH_2OH$ is "consumed" by the cell through passive diffusion, whereas the microelectrode "consumes" $FcCH_2OH$ to produce the $[FcCH_2OH]^+$ that will be regenerated by the cell. The faradaic microelectrode current monitored during SECM imaging inherently contains contributions from both topography and electrochemical activity of the underlying surface. Because the substrate itself does not show any electrochemical activity, the microelectrode

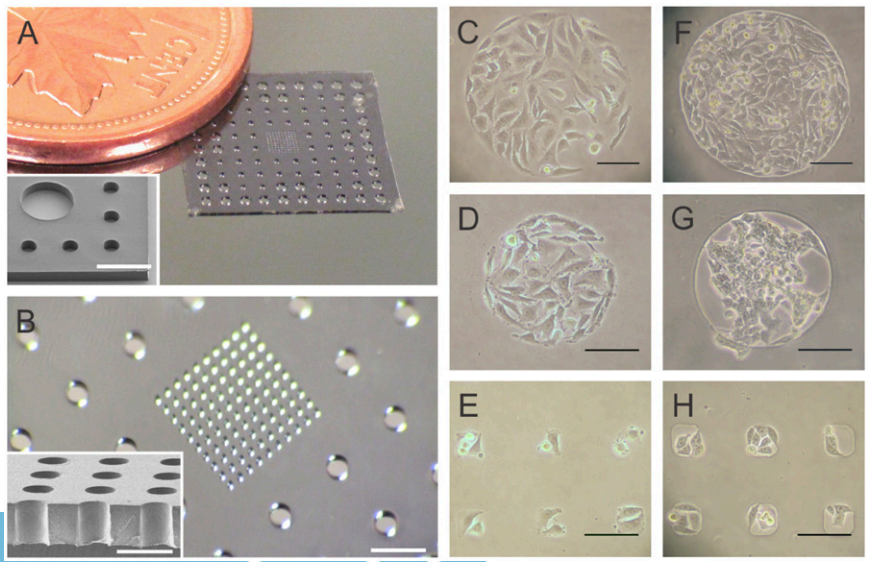

Fig. 1. Layout of the elastomeric stencil and resulting cell patterns. (*A*) Photograph of an open through-hole membrane as used within this study. (*Inset*) Scanning electron micrograph of a corner section. (Scale bar: 500 μm.) (*B*) Close-up view of the central part of the membrane. The array contains 100 openings of 50 μm in diameter arranged in a 10 × 10 configuration. (Scale bar: 500 μm.) (*Inset*) Scanning electron micrograph depicts a cross-sectional view of the array after the membrane had been cut in half using a blade. (Scale bar: 100 μm.) (*C–H*) Optical micrographs of cell islands formed from HeLa (*C–E*) and HeLa-R cells (*F–H*). OPS were generated using circular through-holes of 400 and 200 μm in diameter as well as rectangular features of 50 μm in width and length, respectively. (Scale bar: 100 μm.)

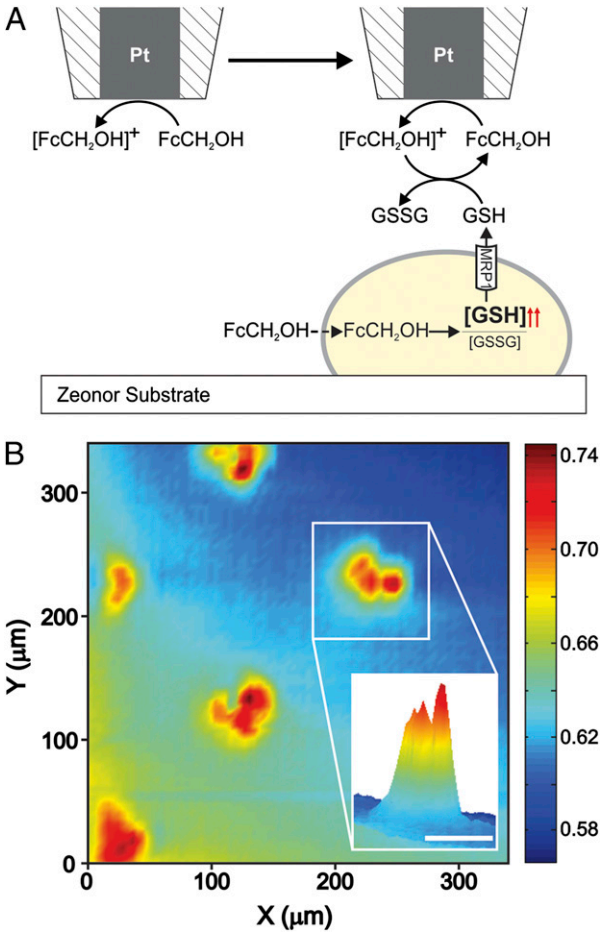

Fig. 2. Cell imaging using SECM. (*A*) Schematic illustration of constant-height feedback mode SECM imaging with a living cell in the presence of $FcCH_2OH$ as a redox mediator. $FcCH_2OH$ is oxidized to $[FcCH_2OH]^+$ at the Pt microelectrode, and regenerated in proximity to the cell as a result of GSH efflux. (*B*) Normalized SECM current recorded at a distance of 12 μm above the substrate when HeLa cells were exposed to $FcCH_2OH$ (1 mM) for 75 min. (*Inset*) Close-up 3D view of the signal obtained from an individual cell island. (Scale bar: 50 μm.)

current progressively decreases with decreasing tip-to-substrate distance as a result of the hindered diffusion of the redox mediator. Using this negative feedback signal, the microelectrode is first prepositioned over a bare region of the substrate at a tip-to-substrate distance greater than the maximum cell height (e.g., 12 μm). The biased microelectrode is then scanned at this constant height across a defined area of patterned cells. As the microelectrode scans over the patterned cells, the measured current monitors the gradient in concentration of $FcCH_2OH$, which is concomitantly affected by the topography of the cell, the cell's permeability to $FcCH_2OH$, and the glutathione-dependent regeneration of $FcCH_2OH$ (Fig. 2*A*). Overall, the contributions from negative feedback and passive $FcCH_2OH$ diffusion into cells are outweighed by the enhanced mass transport contribution of the regeneration reaction of $FcCH_2OH$ (Fig. 2*B*). The SECM image in Fig. 2*B* shows a distinct, well-separated signal for each cell island, which correlates with the original layout of 50-μm features with a spacing of 100 μm in between. The color bar presents the dimensionless microelectrode current Ni_T described as

$$Ni_T = \frac{i_T}{i_{T_\infty}}, \quad [1]$$

where i_T is the measured microelectrode current and $i_{T\infty}$ is the measured microelectrode current in bulk solution. Regions of increased Ni_T over the patterned cells in Fig. 2*B* result from the action of $FcCH_2OH$, which is cell-permeable and alters intracellular glutathione disulfide levels, thereby producing an excess of glutathione (GSH) that is expelled from the cell by MRP1. GSH serves as an antioxidant (Scheme S2) in mammalian cells, and can be used as an indicator for a cell's redox state. Furthermore, its concentration is dependent on MDR (10). The active efflux of GSH from the cell participates in the $FcCH_2OH/[FcCH_2OH]^+$ redox cycle by reducing $[FcCH_2OH]^+$ back to $FcCH_2OH$ (41).

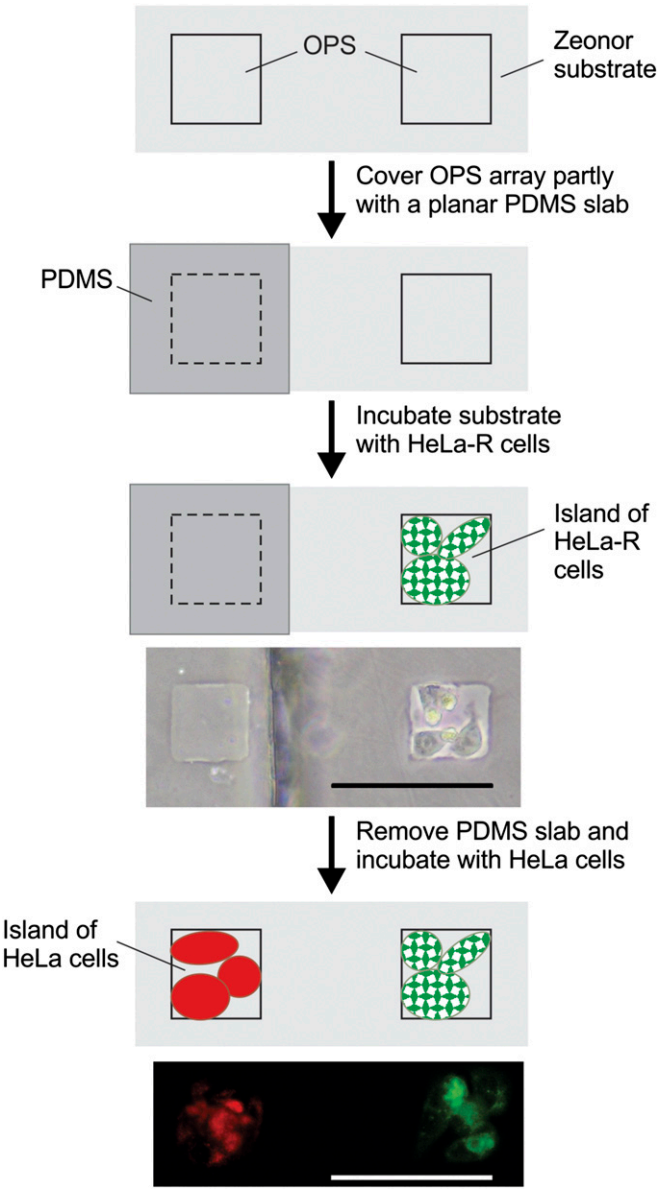

Fig. 3. Formation of cell coculture patterns in a side-by-side configuration. Patterning scheme involves a template partly covered by a PDMS slab to promote selective adhesion and growth of a first cell line (HeLa-R) on the substrate. The optical microscope image depicts an OPS occupied by three HeLa-R cells whereas the adjacent one remains covered by the PDMS slab. Once the slab is removed, the sample is exposed to a second cell line during which cells adhere on OPS that were inaccessible during the first incubation step. The fluorescence micrograph shows stained HeLa cells (red) and HeLa-R cells (green) in the form of a side-by-side coculture pattern. (Scale bar: 100 μm.)

As a result, the flux of $FcCH_2OH$ to the electrode surface increases, leading to a higher electrochemical signal.

Formation of Cell Coculture Patterns. Uniformity of the pattern geometry and chemistry is critical in coculture formation because both parameters can alter the natural morphology and metabolism of the studied cells (42). Within the context of SECM measurements, the dimensions of cocultured patterns should comply with the scan range provided by the instrument to enable simultaneous analysis under identical conditions, which has proven difficult in the past (42–46). We responded to this challenge by partly shielding the template with a thin cover slab of PDMS to produce cocultures of HeLa and HeLa-R cells in a side-by-side format (Fig. 3). During incubation with a first cell line (e.g., HeLa-R), only noncovered OPS are occupied, whereas the PDMS prevents access of the cells to the surface underneath. Once completed, the cell suspension is removed from the substrate, followed by washing and peeling off the PDMS slab. Subsequent incubation with a second cell line (e.g., HeLa) favors adhesion to OPS previously covered by the PDMS slab. The process can also be performed in an alternative fashion by using an open through-hole membrane for incubation, and covering designated sections with PDMS. In principle, this variant would limit the risk of contaminating OPS because PDMS contains low-molecular-weight residues that can be transferred upon contact (47). Dividing an array of 50-μm OPS using a PDMS slab requires alignment, yet the spacing between features was maintained sufficiently large (e.g., 100 μm) to facilitate manual manipulation using a standard microscope setting. A HeLa-R cell pattern with the PDMS slab still in place is included in Fig. 3, demonstrating the ability of the PDMS slab to effectively protect the OPS underneath during the first incubation step. To facilitate discrimination of individual cells in each segment, we performed patterned coculture using HeLa and HeLa-R cells stained with red and green fluorescent dyes, respectively (see *SI Text* for details). Inspection of the patterned sample revealed that it is possible to produce high-quality arrays in which both cell lines remain perfectly separated from each other as shown by the example in Fig. 3. Patterns obtained with 50-μm OPS usually contain 2.8 ± 1.5 HeLa cells and 5.2 ± 2.1 HeLa-R cells. Despite the fact that the number of cells is prone to variation, patterns produced in this way are well suited for quantitative SECM investigation.

SECM Imaging of Cocultures and Data Analysis. We imaged cell cocultures in two different electrochemical solutions to effectively decouple the cell height variability across patterns and quantitatively compare the electrochemical signals produced by each cell line, using the pattern in Fig. 4*A*. The sample comprises HeLa-R (Fig. 4*A*, *Left*) and HeLa cells (Fig. 4*A*, *Right*) free of cross-contamination, as confirmed by the fluorescence image in Fig. 4*B*. To decouple topography from electrochemical activity, the coculture was first imaged in a solution of $[Ru(NH_3)_6]^{3+}$ (Fig. 4*C*), serving as a control, and then in $FcCH_2OH$ solution (Fig. 4*D*) under the same experimental conditions. As a highly charged cation, $[Ru(NH_3)_6]^{3+}$ is a cell-impermeable redox mediator that allows for recording a pure negative feedback response (Fig. 4*C*), which is analogous to surface topography. As the microelectrode is scanned above the patterned cells, the diffusion of $[Ru(NH_3)_6]^{3+}$ to the microelectrode surface is hindered by the physical presence of the cells. Increased cell heights lead to more pronounced decrease in Ni_T. Using pure negative feedback theory and the experimental response of $[Ru(NH_3)_6]^{3+}$, it was possible to transform the SECM current image (Fig. 4*C*) into a topography image (Fig. 4*E*), where the color bar represents the tip-to-substrate distances (micrometers). Wittstock et al. have demonstrated a similar transformation procedure (48). In our study, the dimensional distances were calculated from the normalized tip-to-substrate distances L, which were extracted from the experimental data using the Nelder–Mead simplex algorithm (49) and the analytical approximation for negative feedback current (50)

$$Ni_T^{ins} = \frac{\left(\frac{2.08}{RG^{0.358}}\right)\left(L - \frac{0.145}{RG}\right) + 1.585}{\left(\frac{2.08}{RG^{0.358}}\right)(L + 0.0023RG) + 1.57 + \frac{\ln(RG)}{L} + \left(\frac{2}{\pi RG}\right)\ln\left(1 + \frac{\pi RG}{2L}\right)}, \quad [2]$$

where Ni_T^{ins} is the normalized current over an insulator, L is the normalized distance defined as the ratio of the tip-to-substrate distance and the radius of the metal wire of the electrode, and RG is the ratio of the microelectrode outer radius and metal wire radius. The L values used to calculate the tip-to-substrate distances in Fig. 4*E* were extracted for a microelectrode with $RG = 5.5$, which is within the validity limits of Eq. **2** ($RG < 200$ and all L values). Also, the value of the normalized distance of the first point in the scan (upper left-hand side corner) was 0.92, which corroborates the value extracted from the prepositioning approach curve (0.96). Finally, the slopes in x and y at the edges of the images remained unaltered following the transformation from Fig. 4 *C* to *E*. Although PBS is known to alter cell's morphology and hence its metabolism over time (41), studies on human gastric carcinoma cells have shown a change in cell height of just 55–365 nm when exposed to PBS for a period of 2 h (51). Even when cells were exposed to hypotonic or hypertonic solutions, a height variation of 0.75–2 μm was observed (52). Given an electrode diameter of 25 μm and a significantly more sustaining environment during our studies in cell medium, any possible effect of alteration in cell height lies within the measurement error.

Following this first SECM scan, the $[Ru(NH_3)_6]^{3+}$ solution is removed and replaced by $FcCH_2OH$ solution to acquire a second SECM scan (Fig. 4*D*) using the same experimental conditions. Given the presence of a regeneration reaction, the total normalized microelectrode current Ni_{Tot}, which contains contributions from both cell topography and electrochemical activity, is described by (53, 54)

$$Ni_{Tot} = Ni_s\left(1 - \frac{Ni_T^{ins}}{Ni_T^{cond}}\right) + Ni_T^{ins}, \quad [3]$$

where Ni_s is the kinetically controlled substrate current, Ni_T^{cond} is the normalized current over a conductor, and Ni_T^{ins} is the normalized current over an insulator (see *SI Text* for further details). The behavior of homogeneous reactions toward SECM is not yet described. We assume the reactions to take place mainly in close proximity to the cell surface. Using Eq. **3**, the extracted normalized distances (from Fig. 4*E*), and the Nelder–Mead simplex algorithm, the SECM current image acquired in $FcCH_2OH$ solution (Fig. 4*D*) is converted into a kinetic map

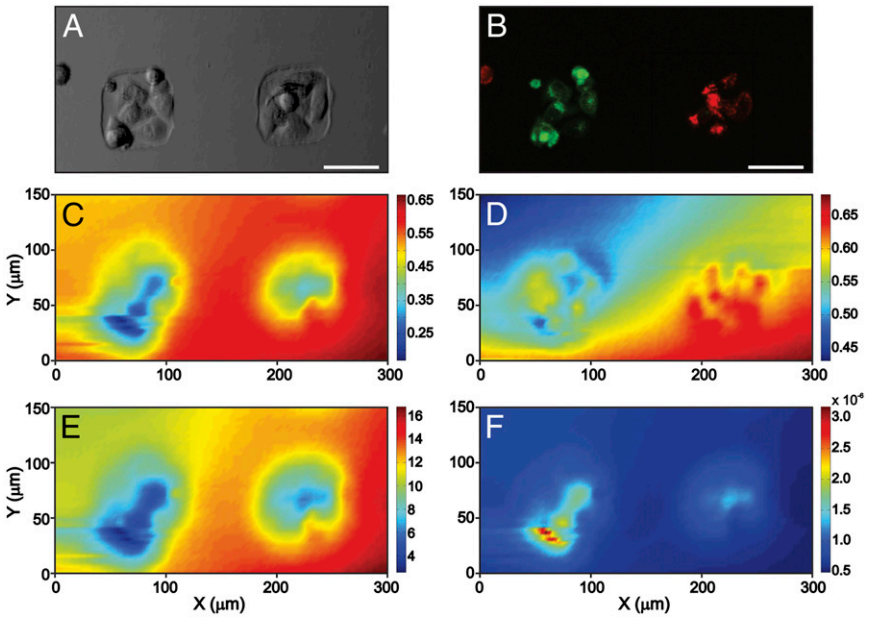

Fig. 4. SECM imaging and decoupling of feedback response for a HeLa and HeLa-R cell coculture substrate. (*A*) Optical micrograph of a coculture pattern containing seven HeLa-R cells (*Left*) and six HeLa cells (*Right*). (*B*) Fluorescence micrograph of the sample shown in *A*, with HeLa-R cells stained green and HeLa cells stained red. (*C* and *D*) Normalized SECM currents recorded with the same sample at 12 μm above the substrate in 1 mM $[Ru(NH_3)_6]^{3+}$ (*C*) and 1 mM $FcCH_2OH$ (*D*). (*E*) Extracted normalized tip-to-substrate distance profile. (*F*) Profile of the extracted apparent heterogeneous rate constant ($cm \cdot s^{-1}$) for the sample shown in *A*. (Scale bar: 50 μm.)

(Fig. 4*F*), where the color bar quantifies the apparent heterogeneous rate constant (k_f). The extracted values for k_f fall within the validity ranges of Eq. **3**, for which $0.1 \leq L \leq 1.5$ and $0.01 \leq \Lambda \leq 1{,}000$ (53). For the bare Zeonor substrate, k_f is on the order of 10^{-7} $cm \cdot s^{-1}$, which is indistinguishable from pure negative feedback behavior. The slope in x and y at the edges of the image on the nonpatterned plastic surface was also insignificant, which demonstrates that the decoupling procedure successfully removed the topographical component from the total current and allowed for the extraction of the kinetic contribution. In comparing the kinetic constants extracted for both patterned cell areas, a clear differential response is observed between normal HeLa cells and their MDR variant. The overall distribution of k_f values over HeLa cells is significantly lower than over their MDR counterparts. Furthermore, the maximum k_f value observed over HeLa-R cells was 2.4 times greater than over HeLa cells (e.g., $k_f = 3.18 \times 10^{-6}$ $cm \cdot s^{-1}$ vs. 1.35×10^{-6} $cm \cdot s^{-1}$, respectively). From Fig. 4*F*, we conclude that the MRP1 phenotype of human cancer cells can be monitored using a nontoxic, electrochemical indicator that causes minimal alterations to the metabolism of the cell.

Conclusions

The SECM measurements presented in this study suggest that it is possible to decouple microelectrode current into two separate profiles for topography and electrochemical activity. The extracellular regeneration of $FcCH_2OH$ was detected and imaged in real time by an SECM microelectrode positioned 12 μm above cell patterns. Comparison of electrochemical signal intensities revealed that a differential response is obtained between HeLa and HeLa-R cells, the latter showing increased activity. The ability to produce cocultures of both HeLa and HeLa-R cells in a spatially controlled manner was essential in this context. The stencil-based patterning method differs from preceding work insofar as it employs a cover slab to control the configuration of the cell culture template, making it accessible for cells on demand in subsequent incubation steps. The relative proximity and regular arrangement of cell islands shortens registration and analysis time. Moreover, this configuration enables multiple experiments to be performed under the exact same microenvironmental conditions, promoting the acquisition of electrochemical data with a high statistical significance. It is possible that this quantitative methodology can be generalized and extended to several adhesive cell lines, given the anticipated versatility of the patterning strategy presented herein. Ideally, we envision a series of cocultured cells having an increasing MRP1 phenotype as obtained through doxorubicin drug challenges (55). The action of selective or competitive MRP1 inhibitors could then be monitored under normal and stressed conditions. Also, the evolution of MDR in cells having an initial low MDR phenotype could be monitored with increasing chemotherapeutic exposure time. In the future, SECM-based methods could indicate the risk of resistance using cells harvested from biopsies. They could be also used for rapid screening of different MDR inhibitors and classify the resistance signature of several cancer cells so that a patient can receive the most appropriate and personalized treatment.

Materials and Methods

Formation of Cell Culture Patterns. For HeLa cell patterning, the Zeonor substrate was first exposed to oxygen plasma and then brought in contact with an untreated elastomeric membrane containing open through-holes (see *SI Text* for further details). The cell culture substrate was placed in a 30-mm Petri dish and fixed using biocompatible high-vacuum grease (Dow Corning). Next, 2.5 mL of $DMEM^+$ was added, followed by removal of air bubbles under reduced pressure for 15 min. A suspension of 5×10^5 cells along with 4 mL of $DMEM^+$ was added to the Petri dish, and the sample was incubated at 37 °C in a 5% (vol/vol) CO_2 atmosphere for 5–24 h. Upon completion of the seeding process, the membrane was peeled off the surface. For HeLa-R cell patterning, the membrane was placed on the Zeonor substrate before treatment with oxygen plasma. The membrane was removed and the Zeonor substrate was placed in a 30-mm Petri dish, followed by addition of a suspension containing 3.5×10^5 cells along with 4 mL of $DMEM^+$. The sample was incubated at 37 °C in a 5% (vol/vol) CO_2 atmosphere for 5–24 h. To obtain coculture patterns, both Zeonor substrate and membrane were exposed to oxygen plasma. The membrane was then removed and the substrate was placed in a 30-mm Petri dish and fixed using biocompatible high-vacuum grease. A section (~50%) of the central array comprising 50-μm OPS was covered using a planar PDMS slab. A cell suspension of 5×10^5 green-stained HeLa-R cells was added and completed to 4 mL with $DMEM^+$. The sample was incubated at 37 °C in a 5% (vol/vol) CO_2 atmosphere for 12 h, followed by washing with $DMEM^-$. Upon removal of the PDMS slab, a suspension of 7×10^5 red-stained HeLa cells was added and completed to 4 mL with $DMEM^+$ if necessary. The sample was incubated at 37 °C in a 5% (vol/vol) CO_2 atmosphere for 14–18 h.

Electrochemical Measurements. Electrochemical imaging was performed in constant-height mode (12 μm above sample normal) at a scan rate of 15

μm·s^{-1} using an Electrochemical Probe Scanner 3 SECM instrument manufactured by HEKA Elektronik Dr. Schulze GmbH (56). Pt microelectrodes (25 μm in diameter) were fabricated and assembled as described previously (41). Oxidation of $FcCH_2OH$ (1 mM dissolved in $DMEM^-$) was recorded at a potential of 0.5 V vs. Ag/AgCl for which a steady-state current was determined using cyclic voltammetry. An electrochemical approach curve was recorded at a speed of 2 μm·s^{-1}. Before electrochemical measurements, HeLa and HeLa-R cells were exposed to 1 mM $FcCH_2OH$ in $DMEM^-$ solution for 75 min. Electrochemical imaging of $[Ru(NH_3)_6]^{3+}$ (1 mM dissolved in $DMEM^-$) reduction was performed at a potential of −0.35 V vs. Ag/AgCl. SECM data were analyzed using Matlab R2012b (MathWorks).

ACKNOWLEDGMENTS. We thank Dr. Philippe Gros (McGill University) for providing the MRP1-overexpressing variant of the HeLa cells, as well as Denis Flipo, Université du Québec à Montréal (UQÀM), Christian Kuss (UQÀM), Caroline Miville-Godin, National Research Council (NRC), and Dr. Teodor Veres (NRC) for technical assistance and useful discussion. This work was supported in part by the Natural Sciences and Engineering Research Council of Canada and the Canadian Foundation for Innovation.

1. Goldstein LJ, Pastan I, Gottesman MM (1992) Multidrug resistance in human cancer. *Crit Rev Oncol Hematol* 12(3):243–253.
2. Persidis A (1999) Cancer multidrug resistance. *Nat Biotechnol* 17(1):94–95.
3. Bourguignon LY, Xia W, Wong G (2009) Hyaluronan-mediated CD44 interaction with p300 and SIRT1 regulates beta-catenin signaling and NFkappaB-specific transcription activity leading to MDR1 and Bcl-xL gene expression and chemoresistance in breast tumor cells. *J Biol Chem* 284(5):2657–2671.
4. Au WY, Chim CS, Wai Lie AK, Pang A, Kwong YL (2002) Real-time quantification of the multidrug resistance-1 gene expression in relapsed acute promyelocytic leukemia treated with arsenic trioxide. *Haematologica* 87(10):1109–1111.
5. Grünebach F, Griese E-U, Schumacher K (1994) Competitive nested polymerase chain reaction for quantification of human *MDR1* gene expression. *J Cancer Res Clin Oncol* 120(9):539–544.
6. Hayashi T, et al. (2004) A competitive nucleic acid sequence-based amplification assay for the quantification of human *MDR1* transcript in leukemia cells. *Clin Chim Acta* 342 (1-2):115–126.
7. Kobayashi H, et al. (2000) Competitive reverse transcription-polymerase chain reaction assay for quantification of human multidrug resistance 1 (*MDR1*) gene expression in fresh leukemic cells. *J Lab Clin Med* 135(2):199–209.
8. Li N, et al. (2008) Absolute quantification of multidrug resistance-associated protein 2 (MRP2/ABCC2) using liquid chromatography tandem mass spectrometry. *Anal Biochem* 380(2):211–222.
9. Li Y, Wang YZ (1998) Competitive RT-PCR assay to quantification of human MDR1 gene expression. *Prog Biochem Biophys* 25(2):146–147.
10. Souslova T, Averill-Bates DA (2004) Multidrug-resistant hela cells overexpressing MRP1 exhibit sensitivity to cell killing by hyperthermia: Interactions with etoposide. *Int J Radiat Oncol Biol Phys* 60(5):1538–1551.
11. Lu H, Gratzl M (1999) Monitoring drug efflux from sensitive and multidrug-resistant single cancer cells with microvoltammetry. *Anal Chem* 71(14):2821–2830.
12. Binyamin L, Assaraf YG, Reiter Y (2005) Probing ATP-dependent conformational changes in the multidrug resistance protein 1 (MRP1/ABCC1) in live tumor cells with a novel recombinant single-chain Fv antibody targeted to the extracellular N-terminus. *Int J Cancer* 116(5):703–709.
13. Feller N, et al. (1995) Functional detection of *MDR*1/P170 and *MRP*/P190-mediated multidrug resistance in tumour cells by flow cytometry. *Br J Cancer* 72(3):543–549.
14. Olson DP, Taylor BJ, Ivy SP (2001) Detection of MRP functional activity: Calcein AM but not BCECF AM as a Multidrug Resistance-related Protein (MRP1) substrate. *Cytometry* 46(2):105–113.
15. Pallis M, Russell NH (1998) Functional multidrug resistance in acute myeloblastic leukaemia: A standardized flow cytometric assay for intracellular daunorubicin accumulation. *Br J Haematol* 100(1):194–197.
16. Mauzeroll J, Schougaard SB (2012) Electrochemical microscopy of living cells. *Scanning Electrochemical Microscopy*, eds Bard AJ, Mirkin MV (Taylor & Francis, London), p 379.
17. Yasukawa T, Kondo Y, Uchida I, Matsue T (1998) Imaging of cellular activity of single cultured cells by scanning electrochemical microscopy. *Chem Lett* 27(8):767–768.
18. Liu B, Cheng W, Rotenberg SA, Mirkin MV (2001) Scanning electrochemical microscopy of living cells: Part 2. Imaging redox and acid/basic reactivities. *J Electroanal Chem* 500(1-2):590–597.
19. Liu B, Rotenberg SA, Mirkin MV (2000) Scanning electrochemical microscopy of living cells: Different redox activities of nonmetastatic and metastatic human breast cells. *Proc Natl Acad Sci USA* 97(18):9855–9860.
20. Mirkin MV, Liu B, Rotenberg SA (2002) Probing redox activity of human breast cells by scanning electrochemical microscopy. *Methods Enzymol* 352:112–122.
21. Rotenberg SA, Mirkin MV (2004) Scanning electrochemical microscopy: detection of human breast cancer cells by redox environment. *J Mammary Gland Biol Neoplasia* 9(4):375–382.
22. Koley D, Bard AJ (2010) Triton X-100 concentration effects on membrane permeability of a single HeLa cell by scanning electrochemical microscopy (SECM). *Proc Natl Acad Sci USA* 107(39):16783–16787.
23. Li X, Bard AJ (2009) Scanning electrochemical microscopy of HeLa cells–Effects of ferrocene methanol and silver ion. *J Electroanal Chem* 628(1-2):35–42.
24. Mauzeroll J, Bard AJ, Owhadian O, Monks TJ (2004) Menadione metabolism to thiodione in hepatoblastoma by scanning electrochemical microscopy. *Proc Natl Acad Sci USA* 101(51):17582–17587.
25. Mauzeroll J, Bard AJ (2004) Scanning electrochemical microscopy of menadione-glutathione conjugate export from yeast cells. *Proc Natl Acad Sci USA* 101(21):7862–7867.
26. Koley D, Bard AJ (2012) Inhibition of the MRP1-mediated transport of the menadione-glutathione conjugate (thiodione) in HeLa cells as studied by SECM. *Proc Natl Acad Sci USA* 109(29):11522–11527.
27. Larbcharoensub N, et al. (2008) Association between multidrug resistance-associated protein 1 and poor prognosis in patients with nasopharyngeal carcinoma treated with radiotherapy and concurrent chemotherapy. *Hum Pathol* 39(6):837–845.
28. Styczynski J, et al. (2007) Predictive value of multidrug resistance proteins and cellular drug resistance in childhood relapsed acute lymphoblastic leukemia. *J Cancer Res Clin Oncol* 133(11):875–893.
29. Luk Y-Y, Kato M, Mrksich M (2000) Self-assembled monolayers of alkanethiolates presenting mannitol groups are inert to protein adsorption and cell attachment. *Langmuir* 16(24):9604–9608.
30. Mrksich M, Dike LE, Tien J, Ingber DE, Whitesides GM (1997) Using microcontact printing to pattern the attachment of mammalian cells to self-assembled monolayers of alkanethiolates on transparent films of gold and silver. *Exp Cell Res* 235(2):305–313.
31. Csucs G, Michel R, Lussi JW, Textor M, Danuser G (2003) Microcontact printing of novel co-polymers in combination with proteins for cell-biological applications. *Biomaterials* 24(10):1713–1720.
32. Wilson WC, Jr., Boland T (2003) Cell and organ printing 1: Protein and cell printers. *Anat Rec A Discov Mol Cell Evol Biol* 272(2):491–496.
33. Beaulieu I, Geissler M, Mauzeroll J (2009) Oxygen plasma treatment of polystyrene and Zeonor: Substrates for adhesion of patterned cells. *Langmuir* 25(12):7169–7176.
34. Takayama S, et al. (1999) Patterning cells and their environments using multiple laminar fluid flows in capillary networks. *Proc Natl Acad Sci USA* 96(10):5545–5548.
35. Folch A, Jo BH, Hurtado O, Beebe DJ, Toner M (2000) Microfabricated elastomeric stencils for micropatterning cell cultures. *J Biomed Mater Res* 52(2):346–353.
36. Tourovskaia A, et al. (2003) Micropatterns of chemisorbed cell adhesion-repellent films using oxygen plasma etching and elastomeric masks. *Langmuir* 19(11):4754–4764.
37. Brassard D, et al. (2011) 3D thermoplastic elastomer microfluidic devices for biological probe immobilization. *Lab Chip* 11(23):4099–4107.
38. Geissler M, Roy E, Diaz-Quijada GA, Galas J-C, Veres T (2009) Microfluidic patterning of miniaturized DNA arrays on plastic substrates. *ACS Appl Mater Interfaces* 1(7): 1387–1395.
39. Roy E, Geissler M, Galas J-C, Veres T (2011) Prototyping of microfluidic systems using a commercial thermoplastic elastomer. *Microfluid Nanofluid* 11(3):235–244.
40. Ostuni E, Kane R, Chen CS, Ingber DE, Whitesides GM (2000) Patterning mammalian cells using elastomeric membranes. *Langmuir* 16(20):7811–7819.
41. Kuss S, et al. (2011) Assessing multidrug resistance protein 1-mediated function in cancer cell multidrug resistance by scanning electrochemical microscopy and flow cytometry. *Bioelectrochemistry* 82(1):29–37.
42. Hu J, et al. (2010) High resolution and hybrid patterning for single cell attachment. *Microelectron Eng* 87(5-8):726–729.
43. Irimia D, Karlsson JOM (2003) Development of a cell patterning technique using poly (ethylene glycol) disilane. *Biomed Microdevices* 5(3):185–194.
44. Ishizaki T, Saito N, Takai O (2010) Correlation of cell adhesive behaviors on superhydrophobic, superhydrophilic, and micropatterned superhydrophobic/superhydrophilic surfaces to their surface chemistry. *Langmuir* 26(11):8147–8154.
45. Jin LH, et al. (2009) Patterning of HeLa cells on a microfabricated Au-coated ITO substrate. *Langmuir* 25(9):5380–5383.
46. Mercey E, et al. (2010) The application of 3D micropatterning of agarose substrate for cell culture and in situ comet assays. *Biomaterials* 31(12):3156–3165.
47. Graham DJ, Price DD, Ratner BD (2002) Solution assembled and microcontact printed monolayers of dodecanethiol on gold: A multivariate exploration of chemistry and contamination. *Langmuir* 18(5):1518–1527.
48. Wittstock G, Emons H, Kummer M, Kirchhoff JR, Heineman WR (1994) Application of scanning electrochemical microscopy and scanning electron microscopy for the characterization of carbon-spray modified electrodes. *Fresenius J Anal Chem* 348(11):712–718.
49. Lagarias J, Reeds J, Wright M, Wright P (1998) Convergence properties of the Nelder–Mead simplex method in low dimensions. *SIAM J Optim* 9(1):112–147.
50. Cornut R, Lefrou C (2007) A unified new analytical approximation for negative feedback currents with a microdisk SECM tip. *J Electroanal Chem* 608(1):59–66.
51. Xue Y, et al. (2010) Real-time monitoring of cell viability by its nanoscale height change with oxygen as endogenous indicator. *Chem Commun (Camb)* 46(39):7388–7390.
52. Liebetrau JM, et al. (2003) Scanning electrochemical microscopy of model neurons: Imaging and real-time detection of morphological changes. *Anal Chem* 75(3):563–571.
53. Mirkin MV, Fan F-RF, Bard AJ (1992) Scanning electrochemical microscopy part 13. Evaluation of the tip shapes of nanometer size microelectrodes. *J Electroanal Chem* 328(1-2):47–62.
54. Wei C, Bard AJ, Mirkin MV (1995) Scanning electrochemical microscopy. 31. Application of SECM to the study of charge transfer processes at the liquid/liquid interface. *J Phys Chem* 99(43):16033–16042.
55. Tada Y, et al. (2002) Increased expression of multidrug resistance-associated proteins in bladder cancer during clinical course and drug resistance to doxorubicin. *Int J Cancer* 98(4):630–635.
56. Cougnon C, Bauer-Espindola K, Fabre DS, Mauzeroll J (2009) Development of a phase-controlled constant-distance scanning electrochemical microscope. *Anal Chem* 81(9): 3654–3659.